Preprints of the 21st IFAC World Congress (Virtual)
Berlin, Germany, July 12-17, 2020

Modal-based Model Predictive Control of Multibody Very Flexible Structures

Marc Artola * **Andrew Wynn** * **Rafael Palacios** *

* *Imperial College London, Exhibition Road, London SW7 2AZ UK (e-mails: marc.artola16@imperial.ac.uk, a.wynn@imperial.ac.uk, r.palacios@imperial.ac.uk).*

Abstract: A model predictive control strategy for flexible multibody structures undergoing large deformations is presented. The dynamics of such structures are highly nonlinear, with local effects introduced by the joint constraints and distributed effects arising from the structure's increased flexibility, from which arbitrary large deflections and rotations can be expected. A modal-based nonlinear reduced order model of an intrinsic description (based on velocities and strains) of geometrically-exact beams is used to underpin the internal model. This low-order model, constructed using the linearised eigenfunctions of the constrained structures, is a set of nonlinear ordinary differential equations in time (i.e. no algebraic equations are present) thus facilitating analysis and demonstrating successful control. Numerical examples are presented based on a very flexible hinged two-link manipulator.

Keywords: Flexible structures, multibody dynamics, nonlinear dynamics, nonlinear MPC

1. INTRODUCTION

Very flexible structures can undergo arbitrarily large deformations and rotations and hence linear models might no longer be accurate enough to describe their dynamics. In the case of flexible beams, where only one of the structure's dimensions is of relevance, the dynamics are governed by a set of nonlinear partial differential equations, as in geometrically-exact beam theories (GEBT, Simo (1985); Reissner (1981)). Here, a particular GEBT description using velocities and strains as primary variables, referred to as an intrinsic formulation (Hodges (2003)), is used to model the three-dimensional structural dynamics.

Joints and hinges are common in applications such as robotics, where arm manipulators are usually modelled by several beam segments attached in different configurations. The joints, displaying wide ranges of motion, are often the main (if not unique) source of nonlinearity, since arm segments are modelled as infinitely rigid links or described by linear models such as Euler-Bernoulli or Timoshenko beam theories, with very few attempts to use nonlinear models, as in Macchelli et al. (2007). However, most of the work focusing on control of such flexible manipulators and structures still relies on assuming linearity in displacements (Le Gorrec et al. (2014); Walsh and Forbes (2015)).

An understanding (and control of) geometrical nonlinearities would facilitate much more complex designs in problems where now linearity is assumed. For instance, control of structures such as satellite foldable antennae (formed by slender, very flexible hinged rods) or cutting-edge gust-alleviating mechanisms in aircraft (consisting of a hinged wing tip segment that can become loose when the vehicle encounters a gust, Castrichini et al. (2016)) would certainly benefit from considering nonlinear effects arising from the increased flexibility.

In the case of spacecraft applications, a relevant control problem might consist in stabilising the structure after having been struck by space debris, while in the second application example, the goal might be to maximise load alleviation by acting on the wing's free section. In either case, the amplitude of the joints is likely to remain small, or at least, minimising it will be a desirable outcome of the control strategy. Hence, nonlinear effects will primarily emerge from large deformations rather than from joint constraints, which are particularly well captured by our low-order model.

The paper is organised as follows. The intrinsic structural model and the technicalities involved in simulating multibody dynamics are discussed in § 2 while the reduced order model, similar to the one portrayed in Artola et al. (2019b) but adapted to account for joints within the structure, is shown in § 3. Nonlinear Model Predictive Control is chosen as our control strategy for its flexibility in handling constraints and accounting for nonlinear dynamics, and a brief description of its implementation is given in § 4. Finally, numerical examples on the simulation and control of multibody structures using the intrinsic formulation are shown in § 5.

2. STRUCTURAL MODEL

2.1 Intrinsic beam equations

The intrinsic formulation of geometrically exact beams of Hodges (2003) describes the structural dynamics with two vector states $\boldsymbol{x}_1(s,t) := [\boldsymbol{v}^\top, \boldsymbol{\omega}^\top]^\top : [0, L] \times \mathbb{R}_+ \to \mathbb{R}^6$ and

⋆ The first author is member of the Innovative Training Network ConFlex. This project has received funding from the European Union's Horizon 2020 research and innovation programme under the Marie Sklodowska-Curie grant agreement No 765579

$\boldsymbol{x}_2(s,t) := [\boldsymbol{f}^\top, \boldsymbol{m}^\top]^\top : [0,L] \times \mathbb{R}_+ \to \mathbb{R}^6$. The first one gathers the translational and angular inertial velocities, $\boldsymbol{v},\ \boldsymbol{\omega} \in \mathbb{R}^3$, while the second gathers the sectional force and moment resultants, $\boldsymbol{f},\ \boldsymbol{m} \in \mathbb{R}^3$. The curvilinear spatial coordinate s defines the elastic axis and t denotes time. L denotes the total arclength of the undeformed and unloaded structures. The equations read

$$M\frac{\partial \boldsymbol{x}_1}{\partial t} - \frac{\partial \boldsymbol{x}_2}{\partial s} - E\boldsymbol{x}_2 + \mathcal{L}_1(\boldsymbol{x}_1)M\boldsymbol{x}_1 + \mathcal{L}_2(\boldsymbol{x}_2)C\boldsymbol{x}_2 = D_0\boldsymbol{x}_1 + D_1\frac{\partial \boldsymbol{x}_1}{\partial s} + D_2\frac{\partial^2 \boldsymbol{x}_1}{\partial s^2} + \boldsymbol{f}_1, \tag{1}$$

$$C\frac{\partial \boldsymbol{x}_2}{\partial t} - \frac{\partial \boldsymbol{x}_1}{\partial s} + E^\top \boldsymbol{x}_1 - \mathcal{L}_1^\top(\boldsymbol{x}_1)C\boldsymbol{x}_2 = 0. \tag{2}$$

All terms are expressed in a local frame of reference ($\boldsymbol{e}_1$, $\boldsymbol{e}_2$, $\boldsymbol{e}_3$ in Fig. 1), with origin at the beam elastic axis and first component of the basis, $\boldsymbol{e}_1$=$[1,0,0]^\top$, tangent to it.

$M(s) : \mathbb{R} \to \mathbb{S}^6_{++}$ and $C(s) : \mathbb{R} \to \mathbb{S}^6_{+}$ are the mass and compliance matrices [1], and the matrix $E(s) : \mathbb{R} \to \mathbb{R}^{6\times 6}$ gathers information on the structure's initial curvature $\boldsymbol{\kappa}_0$ (e.g. arched structures):

$$E = \begin{bmatrix} \widetilde{\boldsymbol{\kappa}}_0 & 0 \\ \widetilde{\boldsymbol{e}}_1 & \widetilde{\boldsymbol{\kappa}}_0 \end{bmatrix}, \tag{3}$$

where the tilde superscript denotes the usual vector product operator $\widetilde{\boldsymbol{a}} \in \mathbb{R}^{3\times 3}$, defined as $\widetilde{\boldsymbol{a}}\boldsymbol{b} = \boldsymbol{a}\times\boldsymbol{b}$, for $\boldsymbol{a},\boldsymbol{b} \in \mathbb{R}^3$. The linear operators $\mathcal{L}_1 : \mathbb{R}^6 \to \mathbb{R}^{6\times 6}$ and $\mathcal{L}_2 : \mathbb{R}^6 \to \mathbb{R}^{6\times 6}$ are defined as

$$\mathcal{L}_1(\boldsymbol{x}_1) = \begin{bmatrix} \widetilde{\boldsymbol{\omega}} & 0 \\ \widetilde{\boldsymbol{v}} & \widetilde{\boldsymbol{\omega}} \end{bmatrix},\ \mathcal{L}_2(\boldsymbol{x}_2) = \begin{bmatrix} 0 & \widetilde{\boldsymbol{f}} \\ \widetilde{\boldsymbol{f}} & \widetilde{\boldsymbol{m}} \end{bmatrix}. \tag{4}$$

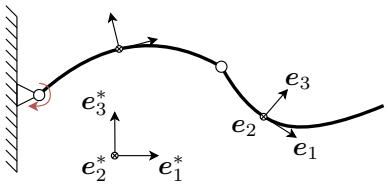

Fig. 1. Frames of reference involved in a multibody hinged configuration.

The vector $\boldsymbol{f}_1$ accounts for external forces and moments per unit length acting on the structure. Matrices D_0, D_1 and D_2 account for structural/viscous damping modelling (Artola et al. (2019b)). Natural boundary conditions (i.e. no internal damping and no boundary forcing) for (1) and (2) satisfy

$$\boldsymbol{x}_1(s_\partial,t)^\top \boldsymbol{x}_2(s_\partial,t) = 0, \tag{5}$$

while forced motions or prescribed forces at a boundary s_∂ are simply enforced as $\boldsymbol{x}_1(s_\partial,t) = \boldsymbol{x}_{1\partial}(t)$ or $\boldsymbol{x}_2(s_\partial,t) = \boldsymbol{x}_{2\partial}(t)$. The total energy (kinetic and potential) of the system is given by

$$\epsilon(t) = \frac{1}{2}\langle \boldsymbol{x}_1, M\boldsymbol{x}_1\rangle + \frac{1}{2}\langle \boldsymbol{x}_2, C\boldsymbol{x}_2\rangle, \tag{6}$$

where $\langle \boldsymbol{x},\boldsymbol{y}\rangle = \int_0^L \boldsymbol{x}^\top \boldsymbol{y} ds$ denotes the $L^2([0,L],\mathbb{R}^6)$-inner product. If (5) holds and no damping is considered, the energy satisfies $\dot{\epsilon} = \langle \boldsymbol{x}_1, \boldsymbol{f}_1\rangle$.

[1] $\mathbb{S}^6_{++}$ and $\mathbb{S}^6_{+}$ denote the set of positive definite and semi-definite symmetric matrices of $\mathbb{R}^{6\times 6}$, respectively.

2.2 Displacements and rotations

Since this is a fully intrinsic description, displacements and rotations are derived variables. Unless required to account for displacement or orientation-dependent external forces (e.g. gravity), they are not needed to solve for (1) and (2).

The rotation matrix from the local to the global frame of reference ($\boldsymbol{e}_1^*$, $\boldsymbol{e}_2^*$, $\boldsymbol{e}_3^*$ in Fig. 1) is $T(s,t) : [0,L] \times \mathbb{R}_+ \to \mathbb{R}^{3\times 3}$. Rotation quaternions are employed to parametrise rotations $\boldsymbol{\xi}(s,t) = [\xi_0, \boldsymbol{\xi}_v^\top]^\top : [0,L] \times \mathbb{R}_+ \to \mathbb{R}^4$, with $\xi_0 \in \mathbb{R}$ and $\boldsymbol{\xi}_v \in \mathbb{R}^3$. They satisfy (Hanson, 2005, ch. 26):

$$\frac{\partial \boldsymbol{\xi}}{\partial s} = \mathcal{U}(\boldsymbol{\kappa} + \boldsymbol{\kappa}_0)\boldsymbol{\xi}, \qquad \frac{\partial \boldsymbol{\xi}}{\partial t} = \mathcal{U}(\boldsymbol{\omega})\boldsymbol{\xi}, \tag{7}$$

where $\boldsymbol{\kappa}$ is the vector of curvatures and twist (i.e. the last three components of the product $C\boldsymbol{x}_2$) and $\mathcal{U}$ is the skew-symmetric operator

$$\mathcal{U}(\boldsymbol{a}) = \frac{1}{2}\begin{bmatrix} 0 & -\boldsymbol{a}^\top \\ \boldsymbol{a} & -\widetilde{\boldsymbol{a}} \end{bmatrix}, \qquad \boldsymbol{a} \in \mathbb{R}^3. \tag{8}$$

The relationship between orientation quaternions and the corresponding rotation matrix is (Hanson, 2005, ch. 6)

$$T(\boldsymbol{\xi}) = (1 - 2\left\|\boldsymbol{\xi}_v\right\|^2)I_{\mathbb{R}^3} + 2\boldsymbol{\xi}_v\boldsymbol{\xi}_v^\top + 2\xi_0\widetilde{\boldsymbol{\xi}}_v, \tag{9}$$

where $I_{\mathbb{R}^3}$ is the identity matrix in $\mathbb{R}^3$. The instantaneous displacement field $\boldsymbol{r}$ with respect to an inertial observer can be computed similarly by solving either of the equations

$$\frac{\partial \boldsymbol{r}}{\partial s} = T(\boldsymbol{e}_1 + \boldsymbol{\gamma}), \qquad \frac{\partial \boldsymbol{r}}{\partial t} = T\boldsymbol{v}, \tag{10}$$

where $\boldsymbol{\gamma}$ is the strain vector (i.e. the first three components of $C\boldsymbol{x}_2$).

2.3 Multibody configurations

To simulate the dynamics of multibody configurations, such as the one portrayed in Fig. 1, an extra set of constraints imposed by the joints/attachments between the diverse structures of the network shall be defined, besides the boundary conditions (5), which are still needed for ends which are not part of any joint.

These constraints, restraining some of the structure's degrees of freedom, shall be translated into the velocity and force/moment variables of the intrinsic formulation. Constraints in displacements or rotations are directly imposed on linear or angular velocities, respectively, noting that these variables are expressed in a body-attached, local frame of reference. Hence, continuity in velocities across the joint has to account for the change in orientation between the joined structures. Constraints for the sectional force/moment are not continuity constraints, as with velocities, but obtained by a force/moment balance at the joint.

The case of a ball joint, where only translational degrees of freedom are constrained leaving all three-dimensional rotations free, with three participating beams is portrayed here as an illustrative example. The constraints imposed on translational velocities are

$$T^a(L^a)\boldsymbol{v}^a(L^a) = T^b(0)\boldsymbol{v}^b(0) = T^c(0)\boldsymbol{v}^c(0),\ t > 0, \tag{11}$$

where T is the transformation matrix (9), and the superscripts denote each of the diverse beams joined together

(see Fig. 2). The force constraint is obtained by a force balance around the joint, that is,

$$-T^a(L^a)\boldsymbol{f}^a(L^a) + T^b(0)\boldsymbol{f}^b(0) + T^c(0)\boldsymbol{f}^c(0) = \mathbf{0},\ t > 0. \tag{12}$$

Note that in (12) the positive direction defined for the spatial coordinate s marks the sign of the force in the balance, as shown in Fig. 2 and also marks the spatial evaluation (0 or end L) of each beam's velocity/force vector in (11)–(12). In the case of a rigid joint between two or more structures, constraints (11)–(12) shall also be equally applied to the angular counterparts $\boldsymbol{\omega}$ and $\boldsymbol{m}$.

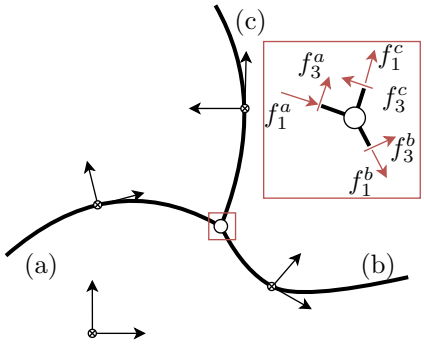

Fig. 2. Example of a three beam network interconnected by a ball joint.

3. LOW-ORDER MODEL

3.1 Modal-based reduced order model

A finite dimensional approximation to the intrinsic equations is built using the eigenfunctions $\boldsymbol{\phi}_{1j}(s)$, $\boldsymbol{\phi}_{2j}(s)$: $[0, L] \to \mathbb{R}^6$ of the linearised system (1)–(2). These are obtained around the unloaded and undeformed configuration (i.e. $\boldsymbol{f}_1 = \boldsymbol{x}_1 = \boldsymbol{x}_2 = \mathbf{0}$) with no damping ($D_i = 0$) and shall comply with boundary conditions (5) and linearised constraints (11)–(12) around a reference angle configuration.

Using N_m eigenfunctions (also referred to as natural modes or mode shapes), approximate state variables are defined by

$$\boldsymbol{x}_1(s,t) = \boldsymbol{\phi}_{1j}(s)q_{1j}(t),\ \boldsymbol{x}_2(s,t) = \boldsymbol{\phi}_{2j}(s)q_{2j}(t), \tag{13}$$

where $q_{1j}(t),\ q_{21j}(t) : \mathbb{R}_+ \to \mathbb{R}$ are the temporal coefficients of the expansion (Einstein's summation convention for index $j = 1, ..., N_m$ is used).

The reduced order model is obtained by a Galerkin projection and has the form

$$\dot{\boldsymbol{q}} = W\boldsymbol{q} + N(\boldsymbol{q})\boldsymbol{q} + \begin{bmatrix} \boldsymbol{\eta} \\ \mathbf{0} \end{bmatrix}, \tag{14}$$

where the expansion temporal coefficients are gathered in a column vector $\boldsymbol{q}(t) : \mathbb{R}_+ \to \mathbb{R}^{2N_m}$. The modes around the unloaded configuration are orthogonal (Palacios (2011)), and if normalised so that $\langle \boldsymbol{\phi}_{1i}, M\boldsymbol{\phi}_{1i} \rangle = \langle \boldsymbol{\phi}_{2i}, C\boldsymbol{\phi}_{2i} \rangle = 1$, the matrix W has the form

$$W = \begin{bmatrix} \Sigma & \Omega \\ -\Omega & 0 \end{bmatrix}, \tag{15}$$

where Ω is a diagonal matrix whose entries are the eigenvalues corresponding to each eigenfunction participating in the expansion and Σ is the modal damping matrix

$$[\Sigma]_{ij} = \left\langle \boldsymbol{\phi}_{1i}, D_0\boldsymbol{\phi}_{1j} + D_1\boldsymbol{\phi}'_{1j} + D_2\boldsymbol{\phi}''_{1j} \right\rangle. \tag{16}$$

The term $N(\boldsymbol{q})$ is linear in $\boldsymbol{q}$,

$$N(\boldsymbol{q}) = \begin{bmatrix} -q_{1l}\Gamma_1^l & -q_{2l}\Gamma_2^l \\ q_{2l}(\Gamma_2^l)^\top & 0 \end{bmatrix}, \tag{17}$$

with constant matrices

$$\left[\Gamma_1^l\right]_{ij} = \langle \boldsymbol{\phi}_{1i}, \mathcal{L}_1(\phi_{1j})M\boldsymbol{\phi}_{1l} \rangle, \tag{18}$$

$$\left[\Gamma_2^l\right]_{ij} = \langle \boldsymbol{\phi}_{1i}, \mathcal{L}_2(\phi_{2j})C\boldsymbol{\phi}_{2l} \rangle. \tag{19}$$

The entries of the forcing term vector are

$$[\boldsymbol{\eta}]_i = \langle \boldsymbol{\phi}_{1i}, \boldsymbol{f}_1 \rangle. \tag{20}$$

The reader is referred to Wynn et al. (2013) for further details on the construction of such model. The instantaneous energy of the system (6) written in modal coordinates is, simply,

$$\epsilon(t) = \frac{1}{2}\boldsymbol{q}^\top\boldsymbol{q}, \tag{21}$$

with ϵ satisfying $\dot{\epsilon} = \boldsymbol{q}_1^\top\boldsymbol{\eta} + \boldsymbol{q}_1^\top\Sigma\boldsymbol{q}_1$.

A similar modal approximation to (13) is defined for the finite rotations, which involves a modal expansion of the quaternions that preserves, weakly, the unit-norm property of rotation quaternions (Artola et al. (2019b)) :

$$\boldsymbol{\xi}(s,t) = \boldsymbol{\phi}_{\xi j}(s)q_{\xi j}(t), \quad j = 0, 1, \cdots, N_m, \tag{22}$$

for chosen quaternion mode shapes $\phi_{\xi j} : [0, L] \to \mathbb{R}^4$, with coefficients $q_{\xi j} : \mathbb{R}_+ \to \mathbb{R}$.

The first mode shape is a *shifting equilibrium mode*, $\boldsymbol{\phi}_{\xi 0} = \bar{\boldsymbol{\xi}}(s)$, where $\bar{\boldsymbol{\xi}}(s)$ defines the undeformed rotation field, that is, $\bar{\boldsymbol{\xi}}' = \mathcal{U}(\boldsymbol{\kappa}_0)\bar{\boldsymbol{\xi}}$.

The remaining modes, $\phi_{\xi j}\ j = 1, \cdots, N_m$, are defined to be the eigenfunctions of the linearised time evolution equation (7) around the unloaded and undeformed condition,

$$\Delta\dot{\boldsymbol{\xi}} = \mathcal{U}_\omega(\bar{\boldsymbol{\xi}})\Delta\boldsymbol{\omega}, \tag{23}$$

where

$$\mathcal{U}_\omega(\bar{\boldsymbol{\xi}}) = \frac{\partial}{\partial\omega}\left(\mathcal{U}(\boldsymbol{\omega})\bar{\boldsymbol{\xi}}\right) = \begin{bmatrix} -\bar{\boldsymbol{\xi}}_v^\top \\ \bar{\boldsymbol{\xi}}_0 I_3 + \tilde{\bar{\boldsymbol{\xi}}}_v \end{bmatrix}. \tag{24}$$

Hence, the mode shapes are obtained from the velocity modes $\boldsymbol{\phi}_{1j}$ by

$$\boldsymbol{\phi}_{\xi j} = \mathcal{U}_\omega(\bar{\boldsymbol{\xi}})\boldsymbol{\phi}_{\omega j}, \quad j = 1, \cdots, N_m, \tag{25}$$

where $\boldsymbol{\phi}_{\omega j} = \Pi_\omega\boldsymbol{\phi}_{1j}$, and $\Pi_\omega = [0_{\mathbb{R}^3}, I_{\mathbb{R}^3}]$ is a projection operator used to retrieve the angular velocity components.

We construct a time evolution system for $\boldsymbol{q}_\xi$ applying a Galerkin projection to the time evolution equation (7) using mode shapes (25) and $\boldsymbol{\phi}_{\xi 0} = \bar{\boldsymbol{\xi}}$:

$$A_\xi\dot{\boldsymbol{q}}_\xi = N_\xi(\boldsymbol{q}_\xi))\boldsymbol{q}_1, \tag{26}$$

where A_ξ and $N_\xi(\boldsymbol{q}_\xi) = q_{\xi l}\Gamma_\xi^l$ are matrices independent of the spatial coordinate s

$$[A_\xi]_{ij} = \left\langle \boldsymbol{\phi}_{\xi i}, \boldsymbol{\phi}_{\xi j} \right\rangle, \tag{27}$$

$$\left[\Gamma_\xi^l\right]_{ij} = \left\langle \boldsymbol{\phi}_{\xi i}, \mathcal{U}(\boldsymbol{\phi}_{\omega j})\boldsymbol{\phi}_{\xi l} \right\rangle. \tag{28}$$

Here, the notation $\langle \cdot, \cdot \rangle$ is used to denote the L^2-inner product in $L^2([0, L], \mathbb{R}^4)$.

The *augmented* low-order model (including finite rotations) reads

$$\dot{\boldsymbol{q}}_a = \begin{bmatrix} W & 0 \\ 0 & 0 \end{bmatrix}\boldsymbol{q}_a + \begin{bmatrix} N(\boldsymbol{q}) & 0 \\ [\, A_\xi^{-1}N_\xi(\boldsymbol{q}_\xi)\ 0\,] & 0 \end{bmatrix}\boldsymbol{q}_a, \tag{29}$$

where $\boldsymbol{q}_a$ is the *augmented* modal coordinates vector $\boldsymbol{q}_a = [\boldsymbol{q}_1^\top, \boldsymbol{q}_2^\top, \boldsymbol{q}_\xi^\top]^\top : \mathbb{R}_+ \to \mathbb{R}^{3N_m+1}$.

3.2 Constrained modes in the intrinsic formulation

As previously described, the low-order model (29) is built using a finite set of eigenfunctions of the linearised and undamped (i.e. $D_i = 0,\ i = 0, 1, 2$) system (1)–(2) around the origin. Using Δ to denote perturbation variables from the linearisation point, the eigenproblem reads

$$\begin{bmatrix} M & 0 \\ 0 & C \end{bmatrix} \frac{\partial}{\partial t} \begin{bmatrix} \Delta \boldsymbol{x}_1 \\ \Delta \boldsymbol{x}_2 \end{bmatrix} = \begin{bmatrix} 0 & E + \partial/\partial s \\ -E^\top - \partial/\partial s & 0 \end{bmatrix} \begin{bmatrix} \Delta \boldsymbol{x}_1 \\ \Delta \boldsymbol{x}_2 \end{bmatrix}. \tag{30}$$

The eigenfunctions which will define the basis onto which the intrinsic equations are projected are obtained by solving (30) together with boundary conditions (5) and the linearised constraints arising from multibody configurations (11)–(12). A FE discretisation, similar to that described for the same equations in Palacios et al. (2010), is used to solve (30), resulting in a constrained eigenvalue problem of the following form

$$\begin{aligned} \lambda B \boldsymbol{X} &= A \boldsymbol{X}, \\ G \boldsymbol{X} &= \boldsymbol{0}, \end{aligned} \tag{31}$$

where $\boldsymbol{X} \in \mathbb{R}^{12N}$ is a vector containing the values of $\boldsymbol{x}_1$ and $\boldsymbol{x}_2$ at each of the N nodes used in the discretisation and $G \in \mathbb{R}^{N_c \times 12N}$ is a constant matrix defining the N_c constraints, including boundary conditions (5) and joint restrictions (11)–(12). This constrained eigenvalue problem can be solved by projecting (31) onto the null space of G, using some transformation matrix Z, so that $\boldsymbol{X} = Z\boldsymbol{X}_p$ and $GZ = 0$ (Gill et al., 1991, §6). Then, the resulting unconstrained eigenproblem is solved, using the projected vector $\boldsymbol{X}_p \in \text{null}(G)$

$$\lambda \left(Z^\top B Z \right) \boldsymbol{X}_p = \left(Z^\top A Z \right) \boldsymbol{X}_p. \tag{32}$$

Using this set of mode shapes to construct the nonlinear low-order model (14), multibody dynamics accounting for nonlinear geometrical effects can be accurately simulated avoiding the use of algebraic equations (or Lagrange multipliers) to enforce constraints, as long as joint angles are sufficiently small. This model provides a low-cost alternative that can suffice for successful control in certain applications, as is exemplified in § 5 with two and three-dimensional stabilisation problems of a very flexible two-link manipulator.

4. NMPC STRATEGY

A conventional nonlinear model predictive strategy is followed, where the solution $\boldsymbol{u}(t)^*$ to the following nonlinear, continuous-time, optimal control problem is used as a control law, which is applied to the system during the time in between samples τ_s,

$$\begin{aligned} \min_{\boldsymbol{u}(t)} & \int_{t_i}^{t_i+\tau_p} V(\boldsymbol{q}_a, \boldsymbol{u}(t)) dt \\ & \boldsymbol{h}(\dot{\boldsymbol{q}}_a, \boldsymbol{q}_a, \boldsymbol{u}(t)) = 0, \\ \text{s.t.} \quad & \boldsymbol{q}_a(t_i) = \boldsymbol{q}_{a_s}, \\ & \boldsymbol{u}_{min} \leq \boldsymbol{u}(t) \leq \boldsymbol{u}_{max}. \end{aligned} \tag{33}$$

Here, τ_p is the prediction time horizon, $\boldsymbol{h}$ represents the ODE (29) and $V(\boldsymbol{q}_a, \boldsymbol{u}(t))$ is a cost functional chosen to have a quadratic form as

$$V = \frac{1}{2} (\boldsymbol{q}_a - \boldsymbol{q}_r)^\top Q (\boldsymbol{q}_a - \boldsymbol{q}_r) + \frac{1}{2} (\boldsymbol{u} - \boldsymbol{u}_r)^\top R (\boldsymbol{u} - \boldsymbol{u}_r), \tag{34}$$

for some weighting matrices $Q \geq 0$ and $R \geq 0$, reference state $\boldsymbol{q}_r$ and control $\boldsymbol{u}_r$. If Q is set equal to the identity, the control can be interpreted to act via energy-shaping, since the state penalty is the perturbed energy of the system. A piece-wise constant parametrisation of the control input $\boldsymbol{u}(t)$ is used, which is independent of the chosen sampling time. The NLP (33) is parametrised employing a multiple shooting strategy (Bock and Krämer-Eis (1984)) and is iteratively solved via Sequential Quadratic Programming, as in Artola et al. (2019a).

A linear model predictive controller is also employed as a means of pinpointing the relevance of capturing nonlinear behaviour arising from large displacements and rotations. This linear version solves the same optimal control problem (33) using a linearised system (29) about a reference equilibrium state $\boldsymbol{q}_r$. Hence, the control policy is obtained at each sample time by solving a quadratic problem (quadratic cost functional plus linear dynamics).

5. NUMERICAL EXAMPLES

5.1 Eigenfunctions for a 2D hinged two-link manipulator

In this section, the eigenfunctions of the planar double-hinge set-up for three different joint angle reference configurations (Fig. 3) are shown.

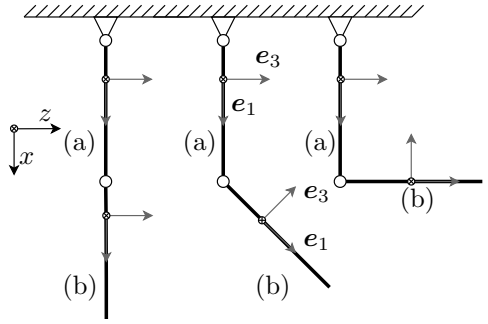

Fig. 3. Planar hinged two-link manipulator with 0°, 45° and 90° joint angle reference configurations.

The five first elastic modes, starting from that of lowest natural frequency, have been computed. The two segments are straight beams of length $L = 1$, with mass $M = \text{diag}(1, 1, 1, 0, 10^{-5}, 0)$ and compliance matrices $C = \text{diag}(1000, \infty, 10^5, \infty, 1, \infty)^{-1}$, all with appropriate units, corresponding to a highly flexible beam in bending with bending-axial geometrical nonlinear couplings.

Fig. 4 shows the spatial distribution of the three components of the velocity modes for this planar case (axial and transverse linear velocities and out-of-plane angular velocity). As observed, the case with 0° joint angle (a) produces mode shapes where axial and transverse motions are completely decoupled (4 pure bending and one pure axial mode). Note how angular velocities are discontinuous across the joint, due to the rotational freedom introduced by the hinge. For the 45° case (b), all modes present axial and transverse motions, with discontinuous linear velocities across the joint, due to the difference in the relative orientation between both beams, according to equation

(11). Finally, the case in which the joint is at an angle of 90° (c) also presents mode shapes where axial and bending motions occur simultaneously, however confined to each of the beams. That is, for each mode, one of the beams undergoes a pure bending motion while the other deforms axially only. The translational velocity mode shapes, superimposed to the reference configuration, are shown in Fig. 5, where the continuity of the velocity vector across the joint is clearly visible.

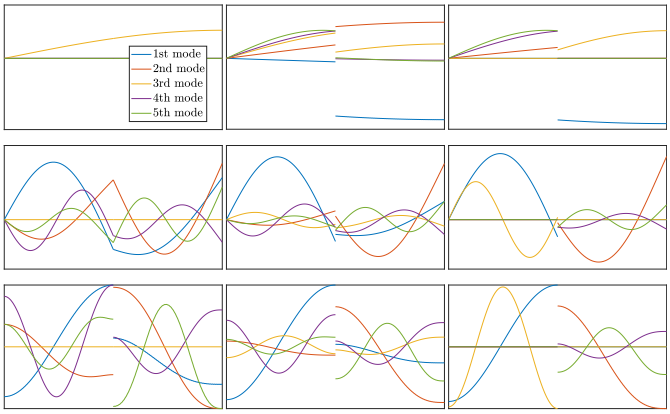

Fig. 4. Spatial distribution of the three different components of the five first elastic velocity modes (ϕ_{v_1},ϕ_{v_3} and ϕ_{ω_2}, top to bottom) for the three different joint reference angles (0° (a), 45° (b) and 90° (c)).

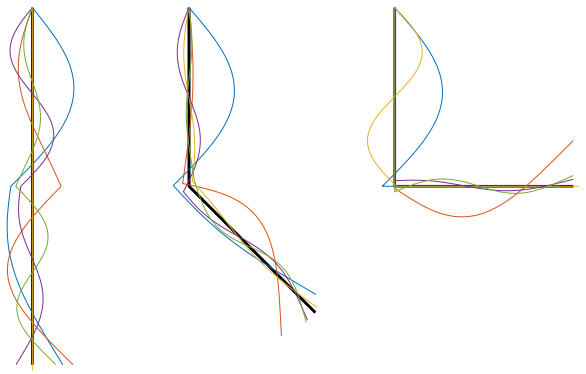

Fig. 5. Comparison of the five first elastic translational velocity mode shapes for the three different joint reference angles (0° (a), 45° (b) and 90° (c)), superimposed to the undeformed structure (thick black line).

5.2 Stabilisation of a hinged two-link manipulator in 2D

The problem is formulated as a disturbance rejection one, in which the structure is initially perturbed by imposing a global rotation velocity of magnitude ω_0 as initial condition. The controller is required to bring the structure back to the origin via three different inputs (torque applied at the hinged root, axial and transverse follower forces applied at the free end) using a functional (34) with the following parameters

$$Q = \text{blkdiag}\left(k_{x_1} I_{\mathbb{R}^{N_m}}, k_{x_2} I_{\mathbb{R}^{N_m}}, K_\xi^\top A_\xi K_\xi + k_{\Delta\xi} A_{\Delta\xi}\right),$$
$$R = k_u I_{\mathbb{R}^3}, \qquad [\boldsymbol{q}_r]_i = 0 \quad i \neq 2N_m + 1, \qquad \boldsymbol{u}_r = \boldsymbol{0}. \tag{35}$$

Here, k_{x_1}, k_{x_2}, $k_{\Delta\xi}$ and k_u are weighting coefficients, K_ξ is a weighting matrix, which allows us to penalise differently the different rotation modes, A_ξ is as in (27) and

$$A_{\Delta\xi} = (\Phi_\xi^a(L^a) - \Phi_\xi^b(0))(\Phi_\xi^a(L^a) - \Phi_\xi^b(0))^\top \tag{36}$$

penalises the relative orientation of both links at the joint with $\Phi_\xi = [\phi_{\xi_0}, \phi_{\xi_1}, \cdots, \phi_{\xi_{N_m+1}}]$ and superscripts denoting each of the two links (as in Fig. 3). References $\boldsymbol{q_r}$ and $\boldsymbol{u}_r$ correspond to the equilibrium state. For $\boldsymbol{q_r}$ all entries are zero except for the *shifting equilibrium* quaternion state, which is $q_{\xi_0,r} = \|\tilde{\boldsymbol{\xi}}(s)\|^{-2}$.

The controlled plant is modelled by an FE discretisation of the intrinsic equations, as the one described in Palacios et al. (2010), with joint restrictions (11)–(12) enforced as hard constraints. This implementation has been verified against a general-purpose finite-element flexible multibody mechanics solver (Del Carre and Palacios (2019)). The model underpinning the MPC is the reduced order model (14) equipped with eight elastic modes (four axial and four bending computed around the 0° joint reference angle) plus the two rigid body modes of the structure. Numerical investigations have been performed to determine a suitable sampling time τ_s (which counteracts mismatch and increases robustness of the scheme) and a suitable prediction time horizon τ_p (which should be long enough to account for the suboptimality error arising from solving a finite-horizon problem).

Results presented below are based on a structure whose parameters are the ones in § 5.1 and a structural damping given by $D_2 = \text{diag}(1,0,0,0,1,0) \cdot 10^{-4}$. MPC parameters are $k_{x_1} = k_{x_2} = 0.01$, $k_{\Delta\xi} = 2.0$, $k_u = 0.1$, $K_\xi = \text{diag}(1,1,1,0.01,\cdots,0.01)$, $\tau_p = 6$ s, $\tau_s = 0.2$ s. A control parametrisation using piecewise constant functions of equally spaced $N_c = 24$ intervals has been chosen and box constraints on the input $|\boldsymbol{u}_{max}| = |\boldsymbol{u}_{min}| = 5$ are imposed.

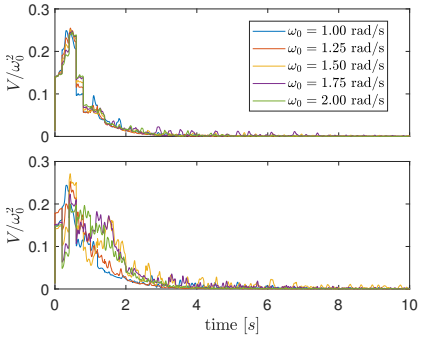

Fig. 6. Objective functional for the LMPC (top) and NMPC (bottom) in the 2D case for different initial disturbances.

The control objective is to stabilise the structure at the initial orientation, aiming to maintain the joint angle as small as possible so that the reduced order model is able to produce control feedback based on sensible predictions. The first objective is achieved by imposing a stronger penalty on the rotations arising from rigid-body modes and deviations of the *shifting equilibrium* rotation mode

from its initial value through matrix K_ξ while the second is achieved by a large tuning constant $k_{\Delta\xi}$.

Fig. 6 shows the scaled functional (34) for both the linear and nonlinear MPC actuaction under different initial excitation, which provides with a metric to assess stabilisation of the system. Both controllers achieve stabilisation over a wide range of initial disturbances. Nonetheless, the nonlinear counterpart displays rather more aggressive behaviour as the perturbation increases, eventually requiring some sub-relaxation within the iterative solution (SQP) of the NLPs for $\omega_0 \gtrapprox 1.75$. This is thought to be caused by the fact that no direct control over the joint angle is exerted, and for a more aggressive actuation the joint angle might be no longer in the range of validity of the model. Hence, the actual state of the structure is no longer well captured by the modes and produces difficulties in converging the corresponding optimisation problems.

As seen in Fig. 7, where the snapshots corresponding to the linear and nonlinear actuation for $\omega_0 = 2.0$ rad/s are compared, larger joint angles are observed in the latter case. The dynamics of the real system present nonlinear effects mainly introduced by the hinge, but also due to axial/bending couplings and follower force effect (note that rotations (7) become linear, with respect $\boldsymbol{\omega}$ or $\boldsymbol{\kappa}$ in a 2D case). These two latter effects are captured by the nonlinear low-order model but they do not appear to dominate the dynamics since the linear counterpart shows good performance throughout the range of tested initial disturbances.

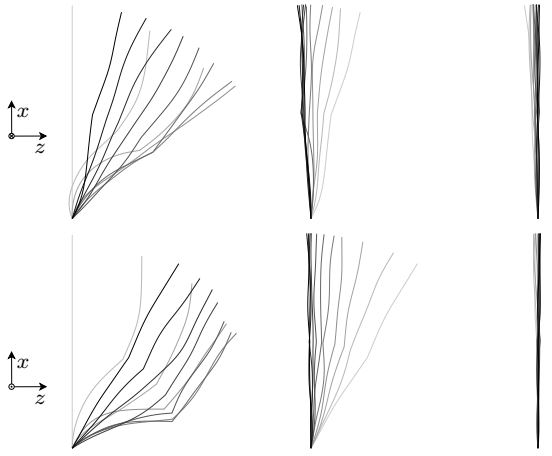

Fig. 7. Snapshots of the 2D two-link every 0.25 s for $t \in [0, 2.5]$ (a), $t \in [2.5, 5]$ (b) and $t \in [5, 7.5]$ s (c). LMPC (top) and NMPC (bottom) results for an initial disturbance of $\omega_0 = 2.0$ rad/s, with shade darkening as t increases.

5.3 Stabilisation of a hinged two-link manipulator in 3D

The three-dimensional problem is set up similarly to the planar one, with structural properties now given by $M = \text{diag}(1, 1, 1, 2 \cdot 10^{-4}, 10^{-4}, 10^{-4})$, compliance matrix $C = \text{diag}(1000, 10^5, 10^5, 0.05, 1, 2)^{-1}$ and $D_2 = \text{diag}(1, 0, 0, 1, 1, 1) \cdot 10^{-4}$, all with appropriate units. The joint is modelled as a double universal joint or wheel joint, which allows for freedom in the two bending directions but is rigid in torsion (i.e. transmits torsion torque and angular velocity). This choice of parameters provides us with a structure displaying increased flexibility in both bending directions and in torsion, with the different bending stiffness producing non-symmetric solutions triggering nonlinear couplings between bending and torsion. The initial angular velocity is applied diagonally, so that it has equal components ω_0 in the y and z directions (resultant disturbance magnitude is $\sqrt{2}\omega_0$). Control inputs are now two follower bending moments at the root and three follower forces applied at the free end, in the three perpendicular directions.

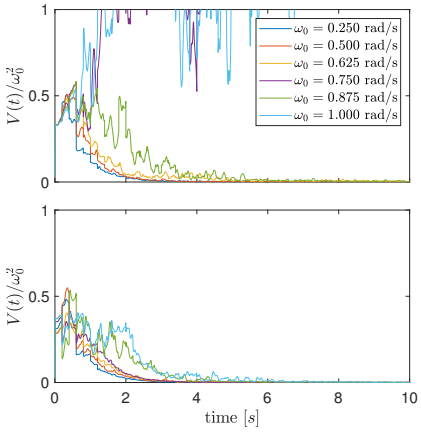

Fig. 8. Objective functional for the LMPC (a) and NMPC (b) in the 3D case for different initial disturbances.

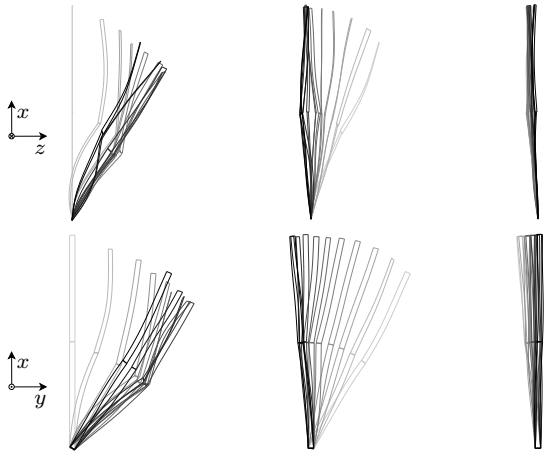

Fig. 9. Snapshots of the 3D two-link every 0.25 s for $t \in [0, 2.5]$ (a), $t \in [2.5, 5]$ (b) and $t \in [5, 7.5]$ s (c). NMPC results for an initial disturbance of $\omega_0 = 1.0$ rad/s, with shade darkening as t increases. Top row refers to the out-of-plane bending, bottom to the in-plane bending.

In this case, the MPC uses a model constructed with a total of sixteen elastic modes (four axial, four torsion and four bending modes in each transverse direction computed around the 0° joint angle configuration) plus the four rigid body modes of the structure. MPC parameters are exactly the same as in the planar case, except for the weighting matrix K_ξ, which now has its first five entries set up equal to one, and R in (35) is now a 5×5 matrix.

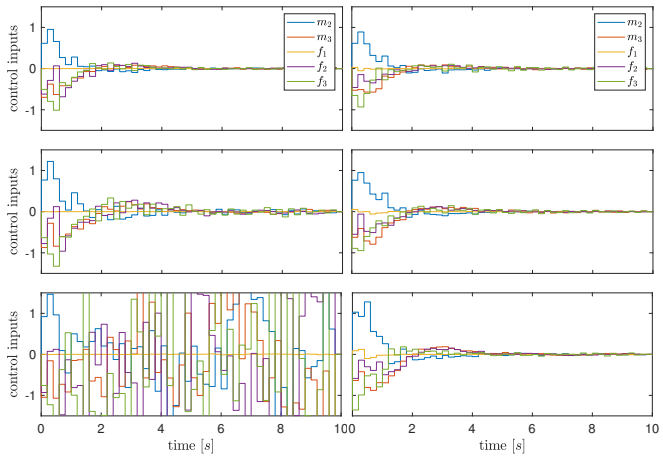

(a) (b)

Fig. 10. Control inputs for LMPC (a) and NMPC (b) actuation for the 3D case, for increasing initial disturbance magnitude ($\omega_0 = 0.5, 0.625, 0.75$ rad/s from top to bottom).

Conversely to the planar case, in the three dimensional scenario the linear controller exhibits failure for relatively low initial disturbance values, when compared to the planar case. This is explained by the fact that there exist strong couplings between both planes that the linear model is unable to predict. This is well observed in Fig. 9, which shows the snapshots for an initial disturbance magnitude of 1.41 rad/s. The in-plane and out-of-plane bending directions of the structure are graphically represented by a beam with a certain width, which helps in visualising the torsion motions too. Fig. 10 shows the inputs produced by both controllers up until the linear one encounters failure, producing a completely chaotic control law. Similarly to the 2D case, the nonlinear counterpart required mild subrelaxation for $\omega_0 \gtrapprox 0.875$ rad/s to achieve convergence of the NLPs.

With three dimensional kinematics, rotations are no longer linear in the intrinsic variables, which explains the poorer authority of the linear controller over the joint angle, in constrast to the nonlinear one. This, and the fact that the follower forces at the tip are highly sensitive to changes in orientation (due to bending/torsion couplings), well captured by the nonlinear low-order model, highlights the necessity for nonlinear control.

6. CONCLUSIONS

In this paper the application of the intrinsic formulation to simulate multibody dynamics has been shown, which presents slight differences with respect to displacement-based formulations due to the use of the extra set of force and moment variables and results in a very compact formulation amenable to model-based control strategies.

Secondly, a computationally efficient (avoids use of algebraic equations to enforce constraints) nonlinear reduced order model for very flexible multibody structures has been presented. This has been shown to provide successful control, underpinning an MPC strategy, in scenarios where geometrical nonlinearities drive the dynamics of the problem and joint rotations are kept within a tolerable margin so that plant/model mismatch is kept to a minimum.

Finally, ongoing investigation focuses on the construction of a (nonlinear) reduced order model obtained by combination of the modes around different joint angles, which possesses two desired characteristics: it preserves the model's structure (physically sensible, energy-preserving) and it expands the model's range of validity, which we deem essential to enhance the controller's performance.

REFERENCES

Artola, M., Wynn, A., and Palacios, R. (2019a). A Nonlinear Modal-Based Framework for Low Computational Cost Optimal Control of 3D Very Flexible Structures. In *2019 18th European Control Conference (ECC)*.

Artola, M., Wynn, A., and Palacios, R. (2019b). Modal-Based Nonlinear Model Predictive Control for 3D Very Flexible Structures. (Under review).

Bock, H. and Krämer-Eis, P. (1984). A Multiple Shooting Method for Numerical Computation of Open and Closed Loop Controls in Nonlinear Systems. *IFAC Proceedings Volumes*, 17(2), 411–415.

Castrichini, A., Hodigere Siddaramaiah, V., Calderon, D.E., Cooper, J.E., Wilson, T., and Lemmens, Y. (2016). Nonlinear folding wing tips for gust loads alleviation. *Journal of Aircraft*, 53(5), 1391–1399.

Del Carre, A. and Palacios, R. (2019). Efficient time-domain simulations in nonlinear aeroelasticity. In *AIAA Scitech 2019 Forum*.

Gill, P., Murray, W., and Wright, M. (1991). *Numerical Linear Algebra and Optimization*. Addison-Wesley.

Hanson, A. (2005). *Visualizing quaternions*. Elsevier.

Hodges, D.H. (2003). Geometrically Exact , Intrinsic Theory for Dynamics of Curved and Twisted Anisotropic Beams. *AIAA Journal*, 41(6), 1131–1137.

Le Gorrec, Y., Macchelli, A., Ramirez, H., and Zwart, H. (2014). Energy shaping of boundary controlled linear port hamiltonian systems. *IFAC Proceedings Volumes*, 47(3), 1580 – 1585. 19th IFAC World Congress.

Macchelli, A., Melchiorri, C., and Stramigioli, S. (2007). Port-Based Modeling of a Flexible Link. *IEEE Transactions on Robotics*, 23(4), 650–660.

Palacios, R. (2011). Nonlinear normal modes in an intrinsic theory of anisotropic beams. *Journal of Sound and Vibration*, 330(8), 1772–1792.

Palacios, R., Murua, J., and Cook, R. (2010). Structural and Aerodynamic Models in Nonlinear Flight Dynamics of Very Flexible Aircraft. *AIAA Journal*, 48(11), 2648–2659.

Reissner, E. (1981). On finite deformations of space-curved beams. *Zeitschrift für angewandte Mathematik und Physik*, 32(32), 734–744.

Simo, J.C. (1985). A Finite Strain Beam Formulation. The Three-Dimensional Dynamic Problem. *Computer Methods in Applied Mechanics and Engineering*, 49(1), 55–70.

Walsh, A. and Forbes, J.R. (2015). Modeling and control of flexible telescoping manipulators. *IEEE Transactions on Robotics*, 31(4), 936–947.

Wynn, A., Wang, Y., Palacios, R., and Goulart, P.J. (2013). An energy-preserving description of nonlinear beam vibrations in modal coordinates. *Journal of Sound and Vibration*, 332(21), 5543 – 5558.